International Journal of Hydrogen Energy 240 (2026) 155481

Contents lists available at ScienceDirect

International Journal of Hydrogen Energy

journal homepage: www.elsevier.com/locate/he

Magnetic effect regulated the Ni–O bond strength of a core-shell CoB@Ni(OH)$_2$ catalyst enhances the oxygen evolution reaction

Lin Wu [a], Lixiang Li [a,*], Han Zhang [a,**], Hongwei Zhao [a], Qingdong Li [b], Xueyuan Zhang [b], Baigang An [a,b,***]

[a] Key Laboratory of Energy Materials and Electrochemistry Research Liaoning Province, School of Chemical Engineering, University of Science and Technology Liaoning, Anshan, 114051, China
[b] Institute of Corrosion Science and Technology, Guangzhou, 510530, China

ARTICLE INFO

Keywords:
Ferromagnetic@Antiferromagnetic coupling
Core-shell structure
Magnetic field-guided spin alignment
Spin polarization
Water oxidation

ABSTRACT

Spintronic catalysis remains largely unexplored for the oxygen evolution reaction (OER). Herein, we propose a novel spin-control strategy by constructing an oriented, 1D core-shell CoB@Ni(OH)$_2$ nanochain architecture. The spin-ordered amorphous ferromagnetic (FM) CoB core effectively induces spin polarization in the antiferromagnetic (AFM) Ni(OH)$_2$ shell via FM@AFM coupling. Combined experimental and theoretical analyses reveal that an applied magnetic field (MF) induces spin alignment in Ni(OH)$_2$. This MF-guided spin alignment triggers directional Ni orbital splitting, promotes d-charge accumulation at Ni–O sites, and activates a switch to the highly efficient lattice oxygen mechanism. Consequently, the CoB@Ni(OH)$_2$ catalyst achieves a low overpotential of 472 mV at 100 mA cm^{-2} and exhibits stability exceeding 150 h under an MF, markedly outperforming its non-magnetic operation. This work demonstrates that engineering FM@AFM interfaces enables the transformation from spin disorder to spin alignment, opening a new avenue for spin-regulated electrocatalytic material design.

1. Introduction

Water splitting is a cornerstone of sustainable energy conversion [1,2], wherein the anodic OER presents a critical kinetic bottleneck due to its complex multi-electron transfer process [3–6]. In recent decades, noteworthy progress has been documented in OER catalysts through techniques such as introducing defects, heteroatom doping, alloying, and crystal facet engineering [7–10]. Fundamentally, O–O bond formation necessitates the cleavage of two O–H bonds, a process driven by spin-electron transfer from diamagnetic hydroxides to form paramagnetic oxygen molecules [11,12]. Consequently, manipulating the spin-state behavior of catalysts can significantly influence the OER process [13].

Traditionally, strategies for improving catalytic activity have been primarily guided by Sabatier's principle, focusing on modulating the binding energy of reaction intermediates. In contrast, approaches employing external field guidance, including the use of light, stress, and magnetic control, are garnering heightened interest for their ability to enhance electrocatalytic efficiency beyond the limitations of the volcano plot [14,15]. In particular, an external magnetic field (MF) can induce spin polarization in catalysts by aligning electron spins, a phenomenon known as the magnetically controlled spin-selective effect [16,17]. This effect influences spin-dependent electron transfer at the solid/liquid interface, thereby potentially altering reaction pathways and enhancing OER kinetics, which offers a route to transcend activity limits predicted by volcano plots [18,19].

To facilitate this mechanism, FM OER catalysts, which promote the spin-selective electron transfer process, have garnered attention within the electrocatalysis community [20]. For instance, field-assisted synthesis can alter the electronic state of Mo, causing a transition of its electrons from the 4d t_{2g} to the degenerate 4d e_g orbitals. This MF regulation of the electronic configuration yields high-performance 1T MoS_2 [21]. Furthermore, a recent investigation has verified that the spin polarization of Mn^{2+} ions within Mn–$CsPbBr_3$ halide perovskite can be

* Corresponding author.
** Corresponding author.
*** Corresponding author. Key Laboratory of Energy Materials and Electrochemistry Research Liaoning Province, School of Chemical Engineering, University of Science and Technology Liaoning, Anshan, 114051, China.
E-mail addresses: lxli@ustl.edu.cn (L. Li), hzhang0807@ustl.edu.cn (H. Zhang), bgan@ustl.edu.cn (B. An).

https://doi.org/10.1016/j.ijhydene.2026.155481
Received 18 January 2026; Received in revised form 22 April 2026; Accepted 8 May 2026
Available online 12 May 2026

augmented by the application of an external MF, which subsequently improves the spin-selective catalytic performance [16]. Recent advances in spin modulation have demonstrated that aligning the spin states of active sites can facilitate the generation of ground-state triplet O_2, thereby fundamentally lowering the kinetic activation barrier [12,22]. This mechanism strongly supports the newly developed concept of catalytic progressivity in OER, wherein the progressive spin alignment dynamically optimizes the thermodynamic energy landscape of oxygen intermediates across consecutive multi-electron transfer steps. However, it should be noted that an external MF does not universally enhance OER for all magnetic materials. For instance, isolated superparamagnetic nanoparticles (e.g., ultrasmall Fe_3O_4 or Co nanoparticles) fail to maintain a stable net magnetic moment at room temperature as thermal fluctuations easily overcome their magnetic anisotropy and randomize the electron spins, even under an applied MF [23]. Similarly, intrinsic antiferromagnetic materials (such as pristine NiO or bare $Ni(OH)_2$) lack macroscopic magnetic responsiveness due to their robust antiparallel spin lattice, preventing the external MF from inducing effective net spin alignment [24]. Consequently, these materials often exhibit a negligible spintronic enhancement during electrocatalytic processes [25]. However, most earth-abundant OER catalysts are AFM at room temperature. Therefore, inducing effective spin polarization in AFM materials is key to leveraging MF enhancements [26,27].

Ni-based (oxy)hydroxides represent state-of-the-art alkaline OER catalysts [28,29], but their AFM nature limits their magnetic responsiveness [30]. Recently, Xu's group demonstrated that constructing FM@AFM core-shell structures (e.g., $Co_{2.75}Fe_{0.25}O_4/Co(Fe)O_xH_y$ and $Fe_3O_4@Ni(OH)_2$) can induce spin polarization at the interface via a spin-pinning effect, providing a strategy to impart FM character to AFM materials [31,32]. Despite these conceptual advances, existing FM@AFM heterostructures are predominantly based on discrete oxide nanoparticles, which often suffer from discontinuous magnetic domains and sluggish interfacial electron transfer, limiting their performance under high current density conditions. Moreover, most reported systems still follow the conventional adsorbate evolution mechanism (AEM), leaving the fundamental switch in catalytic pathways largely unexplored.

Herein, we report a synthetic strategy to construct a uniquely oriented FM@AFM core-shell architecture by controllably coating AFM Ni $(OH)_2$ nanosheets onto amorphous FM CoB nanochains. The exact novelty of this work lies in overcoming the inherent limitation of most earth-abundant OER catalysts (such as Ni-based hydroxides), which are intrinsically AFM and lack magnetic responsiveness at room temperature. By pioneering this integrated FM@AFM interface spin-pinning strategy, the amorphous FM CoB core effectively forces the active AFM $Ni(OH)_2$ shell to become spin-polarized under an external MF. We demonstrate that this field-guided spin polarization not only triggers directional splitting of Ni orbitals but also fundamentally bypasses the scaling relationships of AEM by activating the highly efficient lattice oxygen mechanism. As a result, the $CoB@Ni(OH)_2$ catalyst exhibits a remarkable performance enhancement, bridging the gap between fundamental spintronic theory and high-performance water electrolysis.

2. Experimental section

2.1. Materials

The sodium borohydride ($NaBH_4$, AR), polyvinylpyrrolidone (PVP, M_r. 30000), tetramethylammonium hydroxide solution ($C_4H_{13}NO$, TMAOH), cobalt chloride hexahydrate ($CoCl_2{\cdot}6H_2O$, AR) and nickel chloride hexahydrate ($NiCl_2{\cdot}6H_2O$, AR) were all procured from Aladdin Industrial Co. Ltd., China. All chemical reagents were used as received without any subsequent purification. For all experimental procedures, deionized water was utilized.

2.2. Synthesis of amorphous CoB

To prepare the CoB nanochains, 0.70 mmol of $CoCl_2{\cdot}6H_2O$ was first dissolved in 70 mL of O_2-free deionized water with continuous mechanical stirring. Subsequently, a 70 mL solution of $NaBH_4$ (0.02 M) was introduced dropwise into the aforementioned solution at a controlled rate of approximately 2.0 mL min^{-1} at 4 °C while under a constant MF of approximately 400 mT. After the reaction was complete, the resulting CoB product was washed multiple times with ethanol and ultra-pure water and then subjected to freeze-drying.

2.3. Synthesis of the amorphous-crystalline $CoB@Ni(OH)_2$ structure

For the preparation of $CoB@Ni(OH)_2$, 40 mg of as-prepared CoB was dispersed in a 40 mL solution of 3 mM $NiCl_2{\cdot}6H_2O$, followed by the addition of 3 mL of 25% $NH_3{\cdot}H_2O$ to the suspension. Concurrently, the suspension was subjected to mechanical stirring at a rate of 600 rpm for 1 h. Subsequently, the $CoB@Ni(OH)_2$ was washed with alternating portions of ethanol and double-distilled water, followed by drying under vacuum at 40 °C. To investigate the effect of the AFM shell thickness on the magnetic response, control samples of $CoB@Ni(OH)_2$ with varying shell thicknesses were also synthesized by altering the concentration of the $NiCl_2{\cdot}6H_2O$ solution to 1 mM, 5 mM and 7 mM, while keeping all other synthetic parameters constant.

2.4. Material characterization

An X-ray diffractometer (XRD, D/MAX-2500X) was used to acquire the X-ray diffraction patterns. The sample morphologies were examined using scanning electron microscopy (SEM, Thermo Fisher Scientific Apreos). A transmission electron microscope (TEM, JEM-2010F, JEOL) was employed to obtain high-angle annular dark-field scanning transmission electron microscopic (HAADF-STEM) images and energy dispersion spectra. X-ray photoelectron spectroscopy (XPS, AXIS SUPRA) was utilized for chemical valence analysis, and the spectra were calibrated using the C 1s emission at 284.6 eV as a reference. Raman spectra were collected on a confocal Raman spectroscopic system (Renishaw, Germany) using a 532 nm laser. Magnetic hysteresis loops were measured using a Lakeshore 7404 (Lakeshore, USA) vibrating sample magnetometer (VSM, Quantum Design). Electrochemical activity evaluations were conducted using an electrochemical workstation (CHI 660E, China).

2.5. Electrode preparation

Powder samples with varied magnetic properties (5 mg) were mixed with a 5 wt% Nafion solution (100 μL), deionized water (500 μL) and isopropanol (500 μL). The mixture underwent ultrasonication for 30 min to achieve homogeneity. After sonication, 20 μL of the homogeneous ink was applied onto a glassy carbon electrode (diameter of 6 mm, surface area of 0.2826 cm^2). The loading mass was 0.26 mg cm^{-2}.

2.6. Electrochemical measurements

The electrochemical performance was evaluated using an electrochemical workstation. All tests were performed in a 1.0 M KOH aqueous solution with a three-electrode setup, where a Hg/HgO electrode served as the reference and a Pt mesh was used as the counter electrode. The potentials measured against Hg/HgO were converted to the reversible hydrogen electrode (RHE) scale using the equation: $E_{RHE} = E_{Hg/HgO} + 0.059 \times pH + 0.098$ V. Linear sweep voltammetry (LSV) was conducted at a 5 mV s^{-1} scan rate, with the resulting curves presented without iR correction. The double-layer capacitance was determined from cyclic voltammetry (CV) measurements conducted at various scan rates within the potential window of 1.224 to 1.324 V vs. RHE. In-situ electrochemical impedance spectroscopy (EIS) was performed at various

applied potentials, ranging from the open circuit potential (OCP) to 1.60 V vs. RHE. The measurements were conducted over a frequency range of 100 kHz to 0.1 Hz with a sinusoidal AC perturbation of 5 mV. MFs (0-400 mT) were applied using NdFeB permanent magnets. The intensity was controlled by adjusting the magnet-electrode distance (from 0 to 5.0 cm) and calibrated with a Gauss meter. The MF was applied parallel to the working electrode surface.

2.7. Calculation method

All spin-polarized density functional theory (DFT) calculations [33,34] were carried out in the Vienna ab initio simulation package (VASP) based on the plane-wave basis sets with the projector augmented-wave method [35,36]. The generalized gradient approximation (GGA) with the Perdew-Burke-Ernzerhof (PBE) parametrization was utilized to treat the exchange-correlation potential [37]. To address the inherent deficiencies of GGA, the GGA + U method was incorporated into our calculations. Following a previous study, the effective Hubbard U value for Ni was set to 3.0 eV. To simulate the spin-ordered states, initial magnetic moments were prescribed to Ni atoms to represent both with spin alignment and without spin alignment configurations for comparison. The van der Waals correction of Grimme's DFT-D3 model was also adopted [38]. $Ni(OH)_2$ was modeled with a $2 \times 2 \times 1$ supercell. To eliminate spurious interactions between periodic images, a vacuum layer of 15 Å was applied along the z-direction, and dipole corrections were included. An energy cutoff of 500 eV was applied. A Γ-centered Monkhorst-Pack mesh of $5 \times 5 \times 6$ was employed for Brillouin-zone integration [39]. The structures underwent full relaxation until the energy convergence criterion reached 10^{-5} eV and the maximum force on every atom was below 0.02 eV/Å.

3. Results and discussion

$CoB@Ni(OH)_2$ structures were synthesized using a facile and reliable MF-assisted co-assembly approach, as illustrated in Scheme 1. In the initial stage, cobalt chloride was introduced into an aqueous solution during the polyvinylpyrrolidone (PVP) sol-gel reaction under continuous mechanical stirring to achieve a homogeneous dispersion of Co^{2+} ions. Subsequently, amorphous CoB nanochains were prepared via an MF-assisted wet-chemical reduction process, with PVP serving as the soft template. As shown in Fig. 1a and Fig. S1, the CoB nanochains have a smooth surface and are composed of bead-like particles approximately 200 to 300 nm in size. Due to their high electrical conductivity [40,41], these CoB nanoparticles can act as an optimal support for electron transfer throughout the electrochemical process [42]. Following this, Ni $(OH)_2$ nanosheets were deposited on CoB by a wet-chemical method. SEM images (Fig. 1b and Fig. S2) of $CoB@Ni(OH)_2$ clearly show the sustained chain morphology with uniformly formed $Ni(OH)_2$ on the surface. As shown in the transmission electron microscopy (TEM) images (Fig. 1c), the core-shell structure is distinctly observable. These thin and wrinkled nanosheets of $Ni(OH)_2$ form an interconnected two-dimensional structure that provides continuous and uniform coverage of the entire CoB nanochain surface. As shown in Fig. S3, the thickness of the shell nanosheets covering the core surface is approximately 5-60 nm. The core exhibits no lattice structure, whereas the surface nanosheets exhibit a clear lattice.

High-resolution transmission electron microscopy (HR-TEM) analysis (enlarged in regions I and II in Fig. 1d) revealed that the core is amorphous while the shell is crystalline (corresponding to the $Ni(OH)_2$ (012) crystal face). The selected area electron diffraction pattern (inset in Fig. 1d) reveals the coexistence of diffuse halos and distinct diffraction rings, which can be assigned to the amorphous CoB and crystalline $Ni(OH)_2$ phases, respectively. This observation is in excellent agreement with the XRD results (Fig. 2a) [43]. Furthermore, HAADF-STEM imaging (Fig. 1e) and corresponding elemental mapping reveal a uniform distribution of Co, B, Ni and O elements. The core is composed of Co and B, while the shell is composed of Ni and O. The atomic percentages of Co, Ni, B and O in $CoB@Ni(OH)_2$ are approximately 71.48%, 5.16%, 5.28%, and 18.09%, respectively (Table S1). In summary, these results comprehensively verify the successful fabrication of the $CoB@Ni(OH)_2$ core-shell structure, with $Ni(OH)_2$ nanosheets grown on CoB nanochains.

The crystal structures of $CoB@Ni(OH)_2$ and CoB were examined by XRD, as presented in Fig. 2a. A broad peak is observed at 45°, signifying the amorphous character of the CoB nanochains [44]. After growing Ni $(OH)_2$ layers onto CoB, four additional peaks appeared at approximately 11.2°, 22.5°, 34.2° and 60.5°, corresponding to the (003), (006), (012) and (110) planes of rhombohedral phase α-$Ni(OH)_2$ (JCPDS card No. 38-0715). Crucially, a broad peak similar to that in the XRD pattern of CoB was distinctly observed, suggesting the formation of a

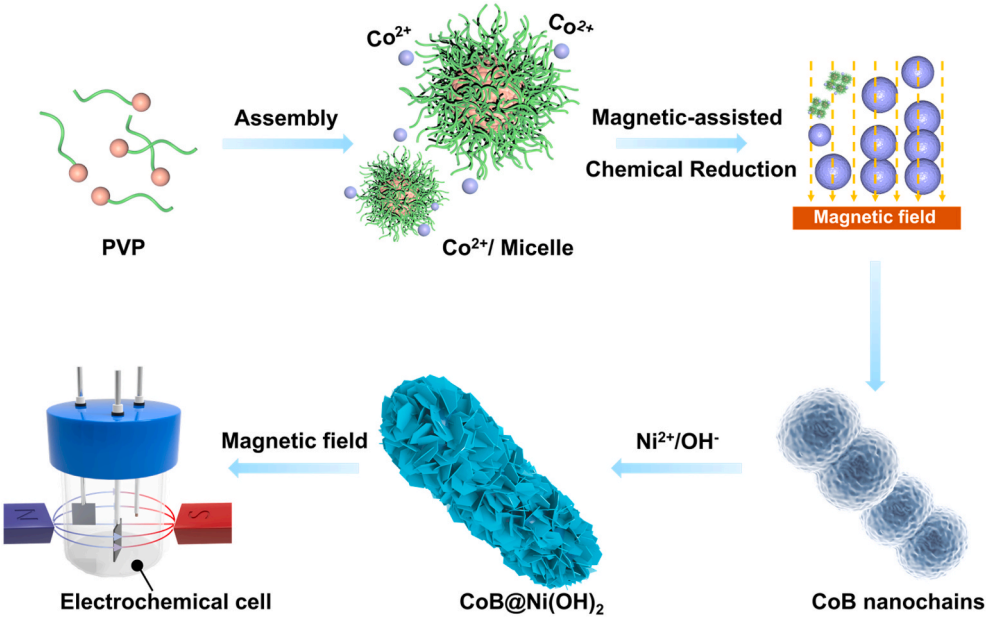

Scheme 1. Schematic illustration of the preparation of the $CoB@Ni(OH)_2$ catalyst.

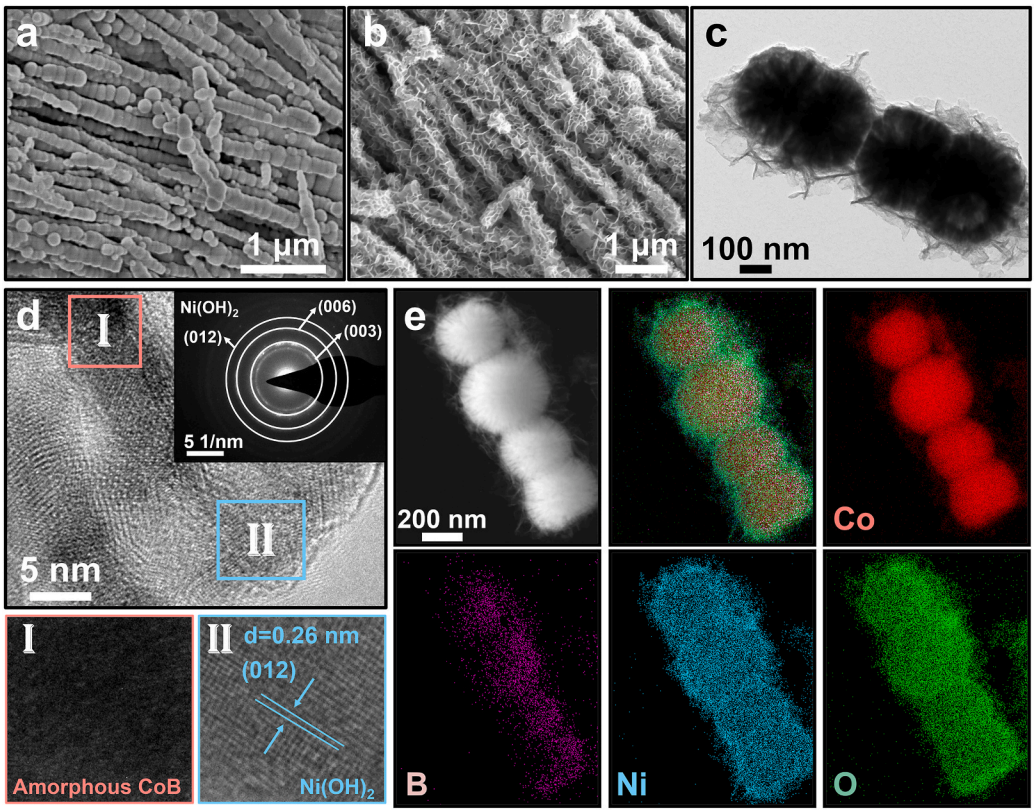

Fig. 1. (a, b) FE-SEM images of CoB and CoB@Ni(OH)$_2$. (c) TEM image of CoB@Ni(OH)$_2$. (d) HR-TEM image of CoB@Ni(OH)$_2$. (e) HAADF-STEM images of CoB@Ni(OH)$_2$ and corresponding elemental maps of Co, B, Ni and O, respectively.

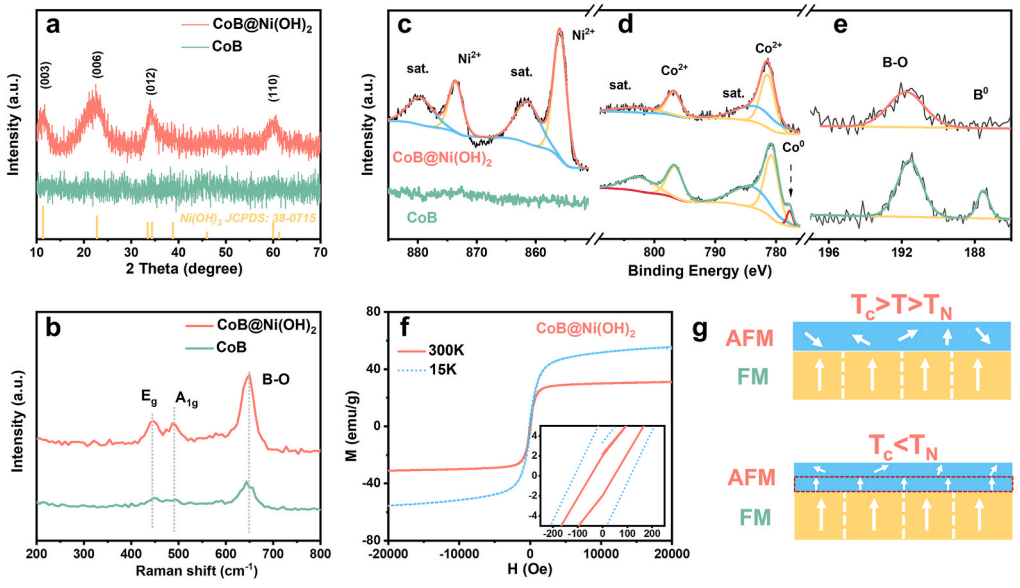

Fig. 2. (a) XRD pattern of CoB and CoB@Ni(OH)$_2$ samples. (b) Raman spectra of CoB and CoB@Ni(OH)$_2$ samples. (c) Ni 2p, (d) Co 2p and (e) B 1s XPS spectra of CoB and CoB@Ni(OH)$_2$. (f) Hysteresis loops of CoB@Ni(OH)$_2$ at 300 K and 15 K. (g) Schematic illustration of spin pinning effect in FM@AFM heterostructure.

heterostructure in CoB@Ni(OH)$_2$. Fig. 2b illustrates the Raman spectral changes during the transition from CoB to CoB@Ni(OH)$_2$. The increase in peak intensity is attributed to the formation of hydroxide. The two characteristic peaks of Ni(OH)$_2$, centered at 455 and 493 cm^{-1}, correspond to the E_g and A_{1g} vibration modes. E_g represents the out-of-plane vibration of the Ni–OH lattice, while A_{1g} signifies the in-plane vibration of the Ni–O lattice.

X-ray photoelectron spectroscopy (XPS) was employed to characterize the chemical and electronic states of the catalysts [44,45]. The existence of Ni, Co, B and O elements is indicated by the XPS survey scan spectra (Fig. S4a). The successful coating of Ni(OH)$_2$ onto the CoB surface, mainly as Ni–O bonds, is confirmed by high-resolution Ni 2p spectroscopy (Fig. 2c). The high-resolution Co 2p spectra (Fig. 2d) exhibit peaks at binding energies of 780.9 and 796.8 eV, corresponding

to the Co $2p_{3/2}$ and Co $2p_{1/2}$ levels of Co^{2+}, which is in agreement with previous reports [46,47]. The Co 2p peak exhibits a positive shift of approximately 0.54 eV toward higher binding energy upon the formation of the $Ni(OH)_2$ shell. This indicates that the Co atoms in CoB@$Ni(OH)_2$ are in an electron-deficient state compared to pristine CoB, suggesting an interfacial charge transfer from CoB to $Ni(OH)_2$. This interfacial effect is further evidenced in the B 1s spectra (Fig. 2e). The distinct peaks for elemental B^0 at 187.5 eV and 191.6 eV in CoB almost completely vanish in CoB@$Ni(OH)_2$, which is attributed to the effective coverage and altered electronic environment induced by the chemically interacting $Ni(OH)_2$ shell. Furthermore, O 1s spectra identify two distinct peaks, one at 531.1 eV corresponding to lattice oxygen species and the other at 532.6 eV associated with adsorbed oxygen species [44,48]. In contrast, CoB has a weak ability to adsorb oxygen species, whereas the adsorption capacity of CoB@$Ni(OH)_2$ is more suitable for OER, a reaction strongly dependent on oxygen species (Fig. S4b) [49,50].

Finally, the magnetic properties were characterized using a VSM. At room temperature, the hysteresis loops confirm that both CoB and CoB@$Ni(OH)_2$ exhibit FM behavior with high saturation magnetizations (M_s, the maximum induced magnetization), reaching 38.9 and 30.1 emu g^{-1}, respectively (Fig. S5). In contrast, pure $Ni(OH)_2$ nanosheets show AFM ordering, reflected in a negligible M_s of only 0.2 emu g^{-1} (Fig. S6). To investigate interfacial coupling, measurements were conducted at 15 K, significantly below the Néel temperature (T_N, critical temperature at which an antiferromagnetic material transitions into a paramagnetic state) of $Ni(OH)_2$ [51], the coercivity (H_c, the reverse field required to reduce magnetization to zero) of CoB@$Ni(OH)_2$ (110.5 Oe) surpasses that at 300 K (35.3 Oe) (Fig. 2f). This enhancement is a direct signature of interfacial exchange coupling. Below T_N, the stabilized spin alignment in the $Ni(OH)_2$ shell couples to the FM CoB core, pinning its magnetization and resulting in the observed increase in H_c and M_s (Fig. 2g) [52]. This spin-polarized interface is magnetically active, meaning that under an applied MF, the interfacial coupling can further align the spin moments. This engineered spin alignment at the interface is anticipated to facilitate the OER by promoting charge transfer and optimizing the adsorption of reaction intermediates [53–55].

The magnetic enhancement effect on the OER of CoB@$Ni(OH)_2$ catalyst was evaluated using a custom-built three-electrode electrochemical cell placed within a permanent magnet and connected to an electrochemical workstation (Fig. S7). Cyclic voltammetry (CV) for these catalysts was performed in alkaline media, both with and without the application of a 400 mT constant MF. As shown in Fig. 3a, the OER performance of CoB@$Ni(OH)_2$ is significantly enhanced with an MF. In stark contrast, the performance of pure FM CoB, pure AFM $Ni(OH)_2$ and non-magnetic IrO_2 catalysts shows negligible change with MF (Fig. S8). A 1.2-fold enhancement in current density is observed for CoB@$Ni(OH)_2$ with MF compared to the case without MF. Similarly, at a current density of 200 mA cm^{-2}, the overpotential decreases by 35 mV (19%) in the presence of the MF compared to its absence, aligning with findings in other FM@AFM-coupled nanoparticles. Furthermore, the overpotential at 100 mA cm^{-2} decreases from 495 to 472 mV, accompanied by a decrease in the Tafel slope under the MF, from 130.2 to 117.4 mV dec^{-1} (Fig. S9). However, the Tafel slopes of CoB and IrO_2 remain virtually unchanged with MF, indicating negligible kinetic enhancement. The decreased Tafel slope of CoB@$Ni(OH)_2$ when an MF is introduced indicates that the rate-determining step in the microkinetic analysis is accelerated during the OER reaction [25,56]. This observation underscores the accelerated reaction kinetics of CoB@$Ni(OH)_2$ with MF.

As shown in Fig. 3a, the Co atoms in CoB transition to a high-valence state during the OER process. This oxidation peak disappears after the growth of $Ni(OH)_2$ nanosheets, while a new pair of Ni^{2+}/Ni^{3+} redox peaks emerges, indicating that $Ni(OH)_2$ serves as the new active site in the FM@AFM structure. Consequently, the FM@AFM coupling, through a MF-induced spin alignment, alters the electron spin polarization on the $Ni(OH)_2$ surface, which in turn impacts the reaction pathway and facilitates oxygen evolution. The MF intensity was accurately manipulated within the range of 0-400 mT, enabling dynamic collection of electrochemical data for the catalysts under varying MF strengths. As shown in Fig. 3b and Fig. S10, electrocatalytic performance is notably improved with increasing MF strength. This enhancement is consistent with facilitated spin-polarized electron transfer promoting reaction kinetics along a more efficient pathway. To unravel the effective depth of the interfacial spin-pinning, we tuned the AFM $Ni(OH)_2$ shell thickness by varying the Ni precursor concentration. As shown in Fig. S11, the magnetic OER enhancement gradually decays with a thicker shell, leading to higher overpotentials. This highlights that the FM@AFM exchange bias possesses a finite penetration depth; an excessively thick shell distances the surface Ni sites from the FM CoB core, thereby preventing spin polarization. Thus, an optimal ultra-thin shell is strictly required to maximize this spintronic catalytic effect. As indicated by the multi-potential step parameter plot for CoB@$Ni(OH)_2$ at 400 mT (Fig. 3c), the current density is approximately 2 to 5 times greater than the value under a zero MF in the potential range of 1.5-1.8 V.

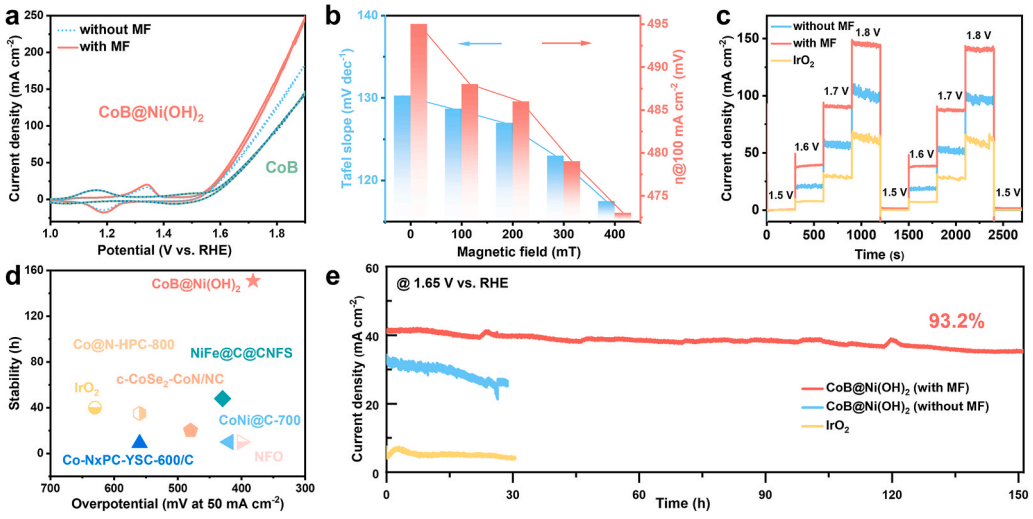

Fig. 3. (a) CV curves of CoB@$Ni(OH)_2$ and CoB in O_2-saturated 1 M KOH with a scan rate of 5 mV s^{-1}. (b) Overpotentials and Tafel slopes of CoB@$Ni(OH)_2$ under different MFs. (c) Multi-potential step parameter plot of the integrated CoB@$Ni(OH)_2$. (d) Comparison of electrocatalytic activity with previously reported non-precious metals electrocatalysts. (e) Current density versus time curves of CoB@$Ni(OH)_2$ compared to IrO_2 catalyst without and with magnetic field (without MF and with MF).

Meanwhile, CoB@Ni(OH)$_2$ at 400 mT exhibits high stability, with the current density decreasing only slightly from 41.5 to 38.7 mA cm^{-2} over 150 h, corresponding to a retention rate of 93.2%. In contrast, the commercial IrO_2 catalyst shows a retention rate of only 34.3% under the same conditions (Fig. 3e). Post-OER characterizations were conducted to confirm the structural and compositional stability of CoB@Ni(OH)$_2$. As shown in Fig. S12, the core-shell nanochain morphology and the amorphous-crystalline interface were well preserved after long-term testing without structural reconstruction. Furthermore, post-OER XPS analysis (Fig. S13) revealed a significant increase in Ni^{3+} active species [57,58], while the Co signal remained largely unchanged, indicating that surface Ni serves as the primary active site. ICP-OES analysis of the electrolyte further verified negligible Co leaching (Fig. S14), confirming that the robust Ni(OH)$_2$ shell effectively protects the underlying CoB core from severe electrochemical corrosion. A comparison of the overpotential and Tafel slope for CoB@Ni(OH)$_2$ with the other reported non-noble metal-based OER electrocatalysts in alkaline media is provided in Fig. 3d and Table S2. The exceptional catalytic activity for water oxidation underscores its substantial potential for practical use in water splitting.

Given its outstanding OER performance, an overall water splitting cell was constructed. With MF, the device exhibits a notably enhanced performance, requiring only 1.72 V to reach 50 mA cm^{-2}, which is 30 mV lower than the value recorded without MF (Fig. S15). At 400 mT, CoB@Ni(OH)$_2$ exhibits a markedly improved OER performance for water splitting, exceeding the current density of commercial IrO_2 across the broad potential range of 1.5-1.8 V (Fig. S16). Therefore, constructing an FM@AFM interfacial coupling proves to be an effective design strategy. It not only creates spin-polarized active sites that are highly responsive to external MFs for superior activity but also ensures exceptional structural and operational stability.

The mechanism investigation of the MF-enhanced OER reveals that the catalytic efficiency can be improved by facilitating gas/liquid mass transport during the reaction and increasing intrinsic activity via spin polarization and spin/magnetic interactions [25,59,60]. To distinguish between these, we first evaluated whether the MF promotes reactant/-product transport by analyzing the electrochemical surface area. The C_{dl} values were comparable with and without an MF (Fig. 4a and Fig. S17-18), indicating that the modulation in OER performance is not due to changes in the electrochemically active area. Further testing under a gradient MF confirms that an increase in OER performance is independent of changes in the catalyst's active area (Fig. 4b and Fig. S19). To rigorously decouple the intrinsic spin-alignment effect from macroscopic physical factors, control experiments with different MF orientations were conducted. The Lorentz force ($F = J \times B$) drives macroscopic mass transport and bubble detachment. While the perpendicular MF yielded slightly higher performance due to the additional Lorentz-force-driven bubble detachment, a highly significant OER enhancement was still unambiguously observed when the MF was applied parallel to the current, a configuration that eliminates the macroscopic Lorentz force (Fig. S20). This, combined with the unaltered in-situ EIS profiles under the parallel MF (Figs. S21–22), proves that this substantial enhancement originates strictly from intrinsic spin physics rather than physical mass transfer or altered bulk conductivity. Thus, the OER enhancement is fundamentally attributed to modifications in the electronic structure of the active sites.

To elucidate the altered OER mechanism, we examined the pH dependence of the activity [61,62]. As shown in Fig. 4c, a strong dependence of OER performance on pH value was observed on the CoB@Ni(OH)$_2$ electrode with MF, while a relatively small dependence was observed without MF. Subsequently, we probed for the involvement of the lattice oxygen oxidation mechanism (LOM) by detecting

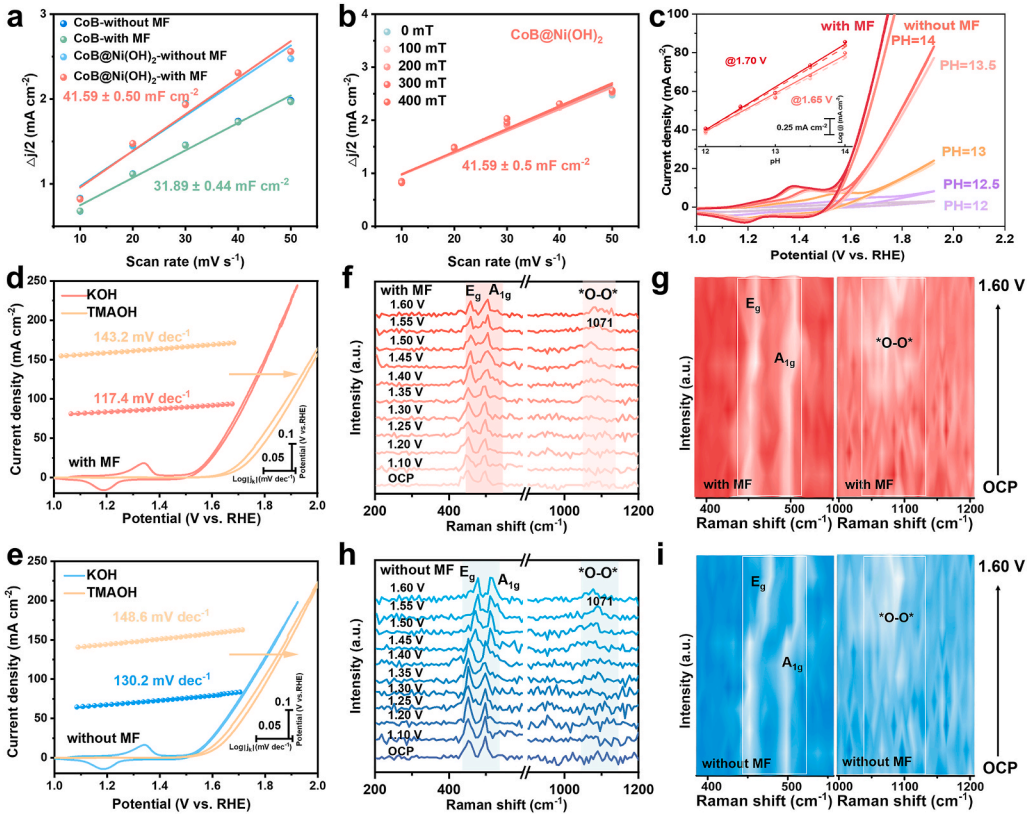

Fig. 4. (a) Plots of Δj/2 vs. scan rates for CoB@Ni(OH)$_2$ and CoB without MF and with MF. (b) Plots of Δj/2 vs. scan rates for CoB@Ni(OH)$_2$ under different MFs. (c) CV curves of the CoB@Ni(OH)$_2$ without MF and with MF at pH 12-14. CV curves of CoB@Ni(OH)$_2$ in 1 M KOH with and without 1 M TMAOH under (d) with MF and (e) without MF conditions. Insets show the corresponding Tafel slopes. The inset is a schematic illustration of pH dependence of CoB@Ni(OH)$_2$. In situ Raman spectra of (f-i) with MF and without MF under various applied potentials (from OCP to 1.60 V vs. RHE).

negatively charged oxygenated species (e.g., peroxo-like O_2^{2-} or superoxo-like O^{2-}). When 1.0 M tetramethylammonium hydroxide (TMAOH) was added in the electrolyte as a chemical probe, the OER activity with MF decreased significantly, and no obvious activity degradation was observed without MF (Fig. 4d and e). With MF, the strong binding of TMA^+ to generated negatively charged oxygen species suggests a stronger LOM contribution to the OER.

Direct evidence for the LOM was obtained through in situ electrochemical Raman spectroscopy. The spectra confirmed the presence of O_2^{2-} species, evidenced by two major peaks at 400-600 cm^{-1} (Fig. 4f and g) corresponding to the δ(M − O) (E_g bending) and ν(M − O) (A_g stretching) vibrations. With an MF, a broad Raman peak assigned to the O–O stretch (ν(*O–O*)) of O_2^{2-} emerges at 1081 cm^{-1} when the potential reaches 1.35 V vs. RHE. In contrast, without an MF, this characteristic O_2^{2-} peak does not appear until a higher potential of 1.40 V vs. RHE and exhibits lower intensity (Fig. 4h and i). The intensity of these O_2^{2-} peaks increases markedly with potential, signifying substantial O_2^{2-} generation and confirming the involvement of LOM during OER. These results collectively suggest that the Ni–O site within $Ni(OH)_2$ is responsible for initiating the LOM pathway for an efficient alkaline OER. Moreover, the application of an MF promotes the involvement of lattice oxygen, thereby enhancing the energy associated with oxygen participation [63, 64]. The robustness of this field-guided spin polarization is further evidenced by a notable effect. The CoB@$Ni(OH)_2$ catalyst retained its enhanced OER performance even immediately upon removal of the external MF (Fig. S23). This sustained enhancement originates from the FM@AFM interfacial exchange bias, where the FM core successfully pins and maintains the spin alignment of the AFM shell. Crucially, this memory effect was subsequently erased by thermal demagnetization, causing the performance to revert to its initial and unmagnetized state. These results provide strong evidence for the robust FM@AFM interfacial spin-pinning mechanism in stabilizing the LOM pathway.

To achieve a deep understanding of the electron transfer mechanisms involved in MF-guided lattice oxygen oxidation, density functional theory (DFT) simulations were performed. In line with the experimental observation of spin alignment, DFT can provide an atomic-level understanding of the origin of this phenomenon in $Ni(OH)_2$ and its contribution to the enhanced OER performance under an MF. The LOM pathway follows a non-concerted proton-electron transfer process, involving sequential steps of OH^- adsorption, O–O coupling, and O_2 release (Fig. 5a). As demonstrated by the DFT calculations, an unpaired Ni 3d electron on the Ni atom induces spin polarization in adjacent O atoms, producing a net spin of approximately 1.60 μ_B for the Ni and its surrounding O atoms (Fig. 5f). The charge density difference reveals electron localization around the O atom along the Ni–O–Ni bond, facilitating charge transfer ability.

A detailed analysis of the electronic structure provides direct evidence for spin alignment. The spin-resolved density of states for the Ni region shows an unequal distribution of spin-up and spin-down electron densities near the Fermi level (E_F). As revealed by the partial density of states (PDOS) in Fig. 5b and Fig. S24, the spin-polarized states in proximity to E_F are derived primarily from the $3d_z^2$ and $3d_{xy/x}^2$ orbitals of Ni, as well as the $3p_x$ and $3p_y$ orbitals of the neighboring O atoms. Analysis of the electron localization function for $Ni(OH)_2$ indicates that the Ni enhances electron delocalization through a significant charge transfer to the surrounding O atoms. According to Hund's rules, the half-

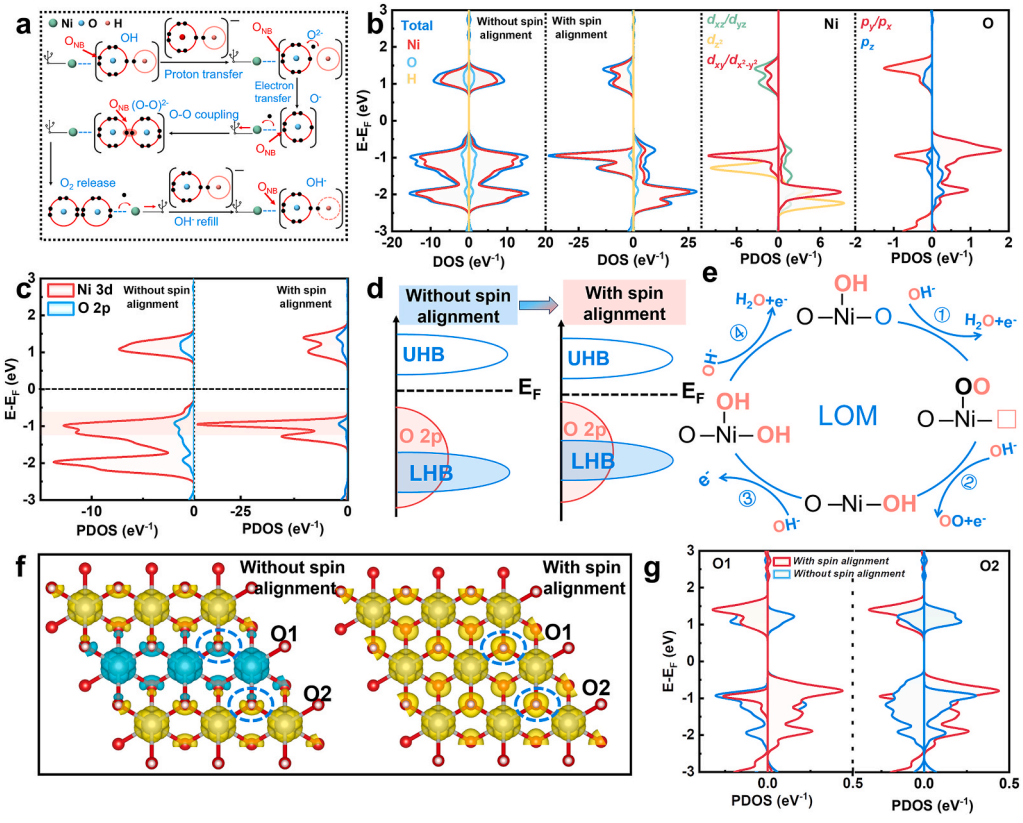

Fig. 5. (a) The electron transfer process in LOM pathway. O_{NB} represents the oxygen non-bonding states. $(O–O)_{2p}$ shows the O–O hybridized band. (b) Total density of states and projected density of states (PDOS) for Ni and neighboring O atoms in $Ni(OH)_2$, calculated without versus with spin alignment. (c) PDOS of $Ni(OH)_2$, and (d) schematic energy bands of $Ni(OH)_2$. (e) Illustration of the proposed comprehensive OER pathway on a $Ni(OH)_2$ catalyst with spin alignment. (f) Spin density plots of $Ni(OH)_2$ without and with spin alignment. Blue and red spheres denote Ni and O atoms, respectively. The yellow and blue isosurfaces represent the spin-up and spin-down states of $Ni(OH)_2$, respectively. A contour map depicting the adsorption energy of a Ni region, with two distinct O sites designated as O1 and O2. (g) PDOS for the O1 and O2 atoms in $Ni(OH)_2$, under conditions with (red) and without (blue) spin alignment at two adjacent Ni sites. (For interpretation of the references to colour in this figure legend, the reader is referred to the Web version of this article.)

filled p_x/p_y orbitals of the O atoms will be populated by two electrons with parallel spins. To enable the transfer of spin-polarized electrons from Ni to O, the spin polarization of O must be opposite to that of the electrons being transferred from Ni. Consequently, the magnetic moment within the adjacent Ni–O–Ni region tends to align with the Ni atoms. These observations suggest that the MF promotes the excitation of electrons in Ni from a low-spin state (3d t_{2g}) to a high-spin state (3d e_g). An increased interleaving is observed between the O 2p and the high-spin-state Ni 3d e_g energy levels (Fig. 5b, Fig. S25-26). This suggests that electrons promoted to the high-spin configuration by the MF can more hybridize with the O 2p band. Critically, as shown by the PDOS in Fig. 5c, the non-bonding orbital of oxygen (O_{NB}) appears near E_F, enabling the oxidation of lattice oxygen atoms [65,66].

Further analysis of the band structure reveals modified bonding characteristics. Under spin polarization, the energy gap between the Ni 3d and O 2p band centers is reduced (Fig. 5d), indicating a stronger covalency of the Ni–O bonds in $Ni(OH)_2$. The O 2p band shifts up toward the E_F compared to the non-spin-polarized case, indicating that the lattice oxygen is more easily oxidized. This shift strongly correlates with our experimental finding that the OER process favors the LOM, a kinetic pathway that is further accelerated by the spin polarization induced in $Ni(OH)_2$ under an applied MF (Fig. 5e).

Mechanistic insights into the transfer of polarized electrons from Ni to O reveal how this process significantly enhances the OER performance of $Ni(OH)_2$ with MF. To examine this phenomenon, two distinct types of O atoms situated in the vicinity of individual Ni sites were designated as O1 and O2 (Fig. 5f). PDOS calculations for two adjacent O atoms at Ni sites, both with and without spin alignment, were performed to simulate this case. Spin polarization enhances the binding affinity between high-spin Ni site electrons and the O 2p orbital, thereby significantly increasing the occupied spin density of O 2p states at the Fermi energy (Fig. 5g). In summary, the enhanced kinetics in the FM@AFM heterostructure can be attributed to the optimized spin density at the Ni–O active sites, achieved through spin alignment in an MF, which results in more favorable adsorption energies for radical intermediates and significantly reduces the reaction barrier.

4. Conclusions

In summary, oriented amorphous FM CoB nanochains were synthesized via a wet-chemical method and utilized as a magnetic substrate to anchor antiferromagnetic (AFM) $Ni(OH)_2$ nanosheets. The resulting CoB@$Ni(OH)_2$ FM@AFM core-shell catalyst demonstrates significantly enhanced OER performance under an external MF, achieving an ultralow overpotential of 472 mV at 100 mA cm^{-2}. This enhancement was unique to the integrated core-shell architecture, as negligible improvement was observed for bare FM CoB under the same field. Magnetic characterization confirms that the core-shell structure exhibits room-temperature ferromagnetism, attributed to interfacial FM@AFM coupling. The enhancement of CoB@$Ni(OH)_2$ OER performance by an MF is attributed to the ferromagnetically induced spin polarization of the surface-active material $Ni(OH)_2$ and the optimized spin density of the Ni active site. The field-regulated Ni–O electronic hybridization fundamentally activates the highly efficient lattice oxygen mechanism. By utilizing the FM@AFM coupling effect and an external MF, magnetic domains are arranged to improve the reaction kinetics, bypassing the traditional scaling relationships. This work offers new insights into the interplay between magnetic spintronic behavior and electrocatalysis, advancing and refining the field of electrocatalytic spintronics.

CRediT authorship contribution statement

Lin Wu: Writing – review & editing, Writing – original draft, Validation, Methodology, Formal analysis, Data curation. **Lixiang Li:** Writing – review & editing, Supervision, Software, Resources, Funding acquisition, Conceptualization. **Han Zhang:** Writing – review & editing, Visualization, Validation, Software, Project administration, Funding acquisition. **Hongwei Zhao:** Project administration, Methodology, Data curation, Conceptualization. **Qingdong Li:** Visualization, Validation, Supervision, Software, Resources. **Xueyuan Zhang:** Supervision, Software, Resources, Project administration, Conceptualization. **Baigang An:** Writing – review & editing, Visualization, Supervision, Software, Conceptualization.

Declaration of competing interest

The authors declare that they have no known competing financial interests or personal relationships that could have appeared to influence the work reported in this paper.

Acknowledgements

Financial support was provided by the National Natural Science Foundation of China No. 51872131, 52371224, 22109061 and the Fundamental Research Funds for the Liaoning Universities, No. LJ222410146062, Key Project supported by the Research Foundation of Education Bureau of Liaoning Province (No. JYTZD2023093).

Appendix A. Supplementary data

Supplementary data to this article can be found online at https://doi.org/10.1016/j.ijhydene.2026.155481.

References

[1] Quan L, Jiang H, Mei G, Sun Y, You B. Bifunctional electrocatalysts for overall and hybrid water splitting. Chem Rev 2024;124:3694–812. https://doi.org/10.1021/acs.chemrev.3c00332.
[2] Eisenberg R, Gray HB, Crabtree GW. Addressing the challenge of carbon-free energy. Proc Natl Acad Sci USA 2020;117:12543–9. https://doi.org/10.1073/pnas.1821674116.
[3] Zhang C, Zheng J, Chen Z, Xu J. Continuous-flow engineered CoMnFe layered double hydroxides with electronically optimized active sites for efficient and stable water oxidation. Adv Funct Mater 2026;36:e19049. https://doi.org/10.1002/adfm.202519049.
[4] Singha Roy S, Minhas H, Lakshminarayanan P, Km K, Sahu S, Pathak B, et al. Vertically grown face-to-face nano-assembly of $In(OH)_3$ and NiFe-LDH enables interfacial charge separation for enhanced alkaline and seawater electrolysis. Adv Funct Mater 2026;36:e24906. https://doi.org/10.1002/adfm.202524906.
[5] Mesa CA, Francas L, Yang KR, Garrido-Barros P, Pastor E, Ma Y, et al. Multihole water oxidation catalysis on haematite photoanodes revealed by operando spectroelectrochemistry and DFT. Nat Chem 2020;12:82–9. https://doi.org/10.1038/s41557-019-0347-1.
[6] Li X, Kuang S, Wang J, Chen Y, Hao J, Lu X, et al. Mo-engineered self-supporting heterostructure of FeNi layered double hydroxide for enhancing oxygen evolution reaction activity and durability in alkaline. Int J Hydrogen Energy 2025;166:150868. https://doi.org/10.1016/j.ijhydene.2025.150868.
[7] Yan D, Xia C, Zhang W, Hu Q, He C, Xia BY, et al. Cation defect engineering of transition metal electrocatalysts for oxygen evolution reaction. Adv Energy Mater 2022;12:2202317. https://doi.org/10.1002/aenm.202202317.
[8] Shi H, Xu X, Gao Y, Chen J, Xu Y, Guo X. Improved electrocatalytic properties of NiFe-LDH by Bi modification. Int J Hydrogen Energy 2025;119:25–33. https://doi.org/10.1016/j.ijhydene.2025.03.262.
[9] Singh A, Kumari P, Shahi RR. $Co_{35}Cr_5Fe_{10}Ni_{30}Ti_5Al_{15-x}Mnx$ (x=0, 7.5) high entropy alloys as electrocatalyst for oxygen evolution reaction. Int J Hydrogen Energy 2025;164:150830. https://doi.org/10.1016/j.ijhydene.2025.150830.
[10] Zhang A-Y, Wang W-Y, Chen J-J, Liu C, Li Q-X, Zhang X, et al. Epitaxial facet junctions on TiO_2 single crystals for efficient photocatalytic water splitting. Energy Environ Sci 2018;11:1444–8. https://doi.org/10.1039/C7EE03482B.
[11] Guo Y, Kloo L, Sun L. Quantum chemical understanding of the O_2 release process from nature's water splitting cofactor. Angew Chem Int Ed 2025;64:e202421383. https://doi.org/10.1002/anie.202421383.
[12] Sun Y, Sun S, Yang H, Xi S, Gracia J, Xu ZJ. Spin-related electron transfer and orbital interactions in oxygen electrocatalysis. Adv Mater 2020;32:2003297. https://doi.org/10.1002/adma.202003297.
[13] Yang Q, Li Y, Kong A, Li Y, An T, Yang C, et al. F-Doping-driven spin reconfiguration in NiFe LDH: unlocking lattice oxygen for high-efficiency oxygen evolution reaction. Appl Catal B Environ Energy 2026;383:126130. https://doi.org/10.1016/j.apcatb.2025.126130.
[14] Cao Y, Gao L, Liu Y, Lin Z. Harnessing magnetic, photo, and thermal fields and their synergistic interactions for enhanced electrocatalytic oxygen evolution reaction. Chem Soc Rev 2026;55:1371–410. https://doi.org/10.1039/D5CS00574D.

[15] Malek A, Wu L, Li Y, Li C, Chen Y, Hazazi K, et al. Transient-promoter-stabilized NiFe oxyhydroxide enables durable kW-scale water splitting under fluctuating power. Angew Chem Int Ed 2026;138:e20825. https://doi.org/10.1002/anie.202520825.
[16] Yuan XY, Guan DH, Wang XX, Li JY, Miao CL, Xu JJ. A magnetic field-assisted lithium-oxygen batteries with enhanced reaction kinetics by spin-polarization strategy. Angew Chem Int Ed 2025;137:e202421361. https://doi.org/10.1002/anie.202421361.
[17] Yu A, Zhang Y, Zhu S, Wu T, Xu ZJ. Spin-related and non-spin-related effects of magnetic fields on water oxidation. Nat Energy 2025;10:435–47. https://doi.org/10.1038/s41560-025-01744-6.
[18] Mtangi W, Tassinari F, Vankayala K, Vargas Jentzsch A, Adelizzi B, Palmans AR, et al. Control of electrons' spin eliminates hydrogen peroxide formation during water splitting. J Am Chem Soc 2017;139:2794–8. https://doi.org/10.1021/jacs.6b12971.
[19] Lv Y, Fang Z, Zhou L, Du P, Gao Z, Zhao W, et al. Beyond volcano top of transition metal-based electrocatalysts triggered by spin state modulation. Adv Funct Mater 2026;36:e20395. https://doi.org/10.1002/adfm.202520395.
[20] Ge J, Ren X, Chen RR, Sun Y, Wu T, Ong SJH, et al. Multi-domain versus single-domain: a magnetic field is not a must for promoting spin-polarized water oxidation. Angew Chem Int Ed 2023;62:e202301721. https://doi.org/10.1002/anie.202301721.
[21] Ding W, Hu L, Dai J, Tang X, Wei R, Sheng Z, et al. Highly ambient-stable 1T-MoS_2 and 1T-WS_2 by hydrothermal synthesis under high magnetic fields. ACS Nano 2019;13:1694–702. https://doi.org/10.1021/acsnano.8b07744.
[22] Ren X, Wu T, Sun Y, Li Y, Xian G, Liu X, et al. Spin-polarized oxygen evolution reaction under magnetic field. Nat Commun 2021;12:2608. https://doi.org/10.1038/s41467-021-22865-y.
[23] Neuberger T, Schöpf B, Hofmann H, Hofmann M, von Rechenberg B. Superparamagnetic nanoparticles for biomedical applications: possibilities and limitations of a new drug delivery system. J Magn Magn Mater 2005;293:483–96. https://doi.org/10.1016/j.jmmm.2005.01.064.
[24] Jungwirth T, Marti X, Wadley P, Wunderlich J. Antiferromagnetic spintronics. Nat Nanotech 2016;11:231–41. https://doi.org/10.1038/nnano.2016.18.
[25] Garcés-Pineda FA, Blasco-Ahicart M, Nieto-Castro D, López N, Galán-Mascarós JR. Direct magnetic enhancement of electrocatalytic water oxidation in alkaline media. Nat Energy 2019;4:519–25. https://doi.org/10.1038/s41560-019-0404-4.
[26] Wang X, Pi W, Hu S, Bao H, Yao N, Luo W. Boosting oxygen evolution reaction performance on NiFe-based catalysts through d-orbital hybridization. Nano-Micro Lett 2025;17:11. https://doi.org/10.1007/s40820-024-01528-9.
[27] Kuai C, Liu L, Hu A, Zhang Y, Zhang Y, Xia D, et al. Dissolved Fe species enable a cooperative solid-molecular mechanism for the oxygen evolution reaction on NiFe-based catalysts. Nat Catal 2025;8:523–35. https://doi.org/10.1038/s41929-025-01342-5.
[28] Liu S, Jia B, Wang Y, Zhao Y, Liu L, Fan F, et al. Topological synthesis of 2D high-entropy multimetallic (oxy)hydroxide for enhanced lattice oxygen oxidation mechanism. Adv Mater 2024;36:2409530. https://doi.org/10.1002/adma.202409530.
[29] Jia H, Wang H, Yan F, Li Z, Li R, Li S, et al. Fe dimers incorporated within $Ni(OH)_2$ nanosheets to enable rapid oxygen radical coupling and exceptional durability in oxygen evolution. Appl Catal B Environ Energy 2025;364:124861. https://doi.org/10.1016/j.apcatb.2024.124861.
[30] Železný J, Wadley P, Olejník K, Hoffmann A, Ohno H. Spin transport and spin torque in antiferromagnetic devices. Nat Phys 2018;14:220–8. https://doi.org/10.1038/s41567-018-0402-7.
[31] Wu T, Ren X, Sun Y, Sun S, Xian G, Scherer GG, et al. Spin pinning effect to reconstructed oxyhydroxide layer on ferromagnetic oxides for enhanced water oxidation. Nat Commun 2021;12:3634. https://doi.org/10.1038/s41467-021-23896-1.
[32] Ge J, Chen RR, Ren X, Liu J, Ong SJH, Xu ZJ. Ferromagnetic-antiferromagnetic coupling core-shell nanoparticles with spin conservation for water oxidation. Adv Mater 2021;33:2101091. https://doi.org/10.1002/adma.202101091.
[33] Benites M, Rosado A, Manousakis E. Gradient-expansion of the inhomogeneous electron gas revisited. Phys Rev B 2026;113:115136. https://doi.org/10.1103/mhrq-s8wr.
[34] Kohn W, Sham LJ. Self-consistent equations including exchange and correlation effects. Phys Rev 1965;140:A1133–8. https://doi.org/10.1103/PhysRev.140.A1133.
[35] Kresse G, Furthmüller J. Efficient iterative schemes for ab initio total-energy calculations using a plane-wave basis set. Phys Rev B 1996;54:11169. https://doi.org/10.1103/PhysRevB.54.11169.
[36] Engel M, Marsman M, Franchini C, Kresse G. Electron-phonon interactions using the projector augmented-wave method and wannier functions. Phys Rev B 2020;101:184302. https://doi.org/10.1103/PhysRevB.101.184302.
[37] Perdew JP, Burke K, Ernzerhof M. Generalized gradient approximation made simple. Phys Rev Lett 1996;77:3865. https://doi.org/10.1103/PhysRevLett.77.3865.
[38] Grimme S, Antony J, Ehrlich S, Krieg H. A consistent and accurate ab initio parametrization of density functional dispersion correction (DFT-D) for the 94 elements H-Pu. J Chem Phys 2010;132:154104. https://doi.org/10.1063/1.3382344.
[39] Kresse G, Furthmüller J. Brillouin-zone integration by fourier quadrature: special points for superlattice and supercell calculations. Phys Rev B 1989;39:3168. https://doi.org/10.1103/PhysRevB.39.3168.
[40] Ma J-l, Li N, Zhang Q, Zhang X-b, Wang J, Li K, et al. Synthesis of porous and metallic CoB nanosheets towards a highly efficient electrocatalyst for rechargeable Na-O_2 batteries. Energy Environ Sci 2018;11:2833–8. https://doi.org/10.1039/C8EE01472H.
[41] Zhang Y, Wang J, Zhang Y, Zheng Q, Wang L, Jiang W. Breaking the trade-off between electrical conductivity and mechanical strength in bulk graphite using metal-organic framework-derived precursors. Adv Sci 2025;12:2416210. https://doi.org/10.1002/advs.202416210.
[42] Yan J, Wang H, Ji S, Pollet BG, Wang R. Achieving highly practical capacitance of MnO_2 by using chain-like CoB alloy as support. Nanoscale 2018;10:7813–20. https://doi.org/10.1039/C8NR01004H.
[43] Ma Y, Wang R, Wang H, Linkov V, Ji S. Evolution of nanoscale amorphous, crystalline and phase-segregated PtNiP nanoparticles and their electrocatalytic effect on methanol oxidation reaction. Phys Chem Chem Phys 2014;16:3593–602. https://doi.org/10.1039/C3CP54600D.
[44] Nsanzimana JMV, Gong L, Dangol R, Reddu V, Jose V, Xia BY, et al. Tailoring of metal boride morphology via anion for efficient water oxidation. Adv Energy Mater 2019;9:1901503. https://doi.org/10.1002/aenm.201901503.
[45] Zhang Y, Wang Z, Xiao X, Xiang Y, Gao R, Ge W, et al. Fe and S Co-doping in CeO_2/$Co(OH)_2$ heterostructure as an ampere-level active and stable electrocatalyst for the oxygen evolution reaction. Int J Hydrogen Energy 2025;138:468–76. https://doi.org/10.1016/j.ijhydene.2025.05.118.
[46] He D, Song X, Li W, Tang C, Liu J, Ke Z, et al. Active electron density modulation of Co_3O_4-based catalysts enhances their oxygen evolution performance. Angew Chem Int Ed 2020;59:6929–35. https://doi.org/10.1002/anie.202003609.
[47] Liu J, Ji Y, Nai J, Niu X, Luo Y, Guo L, et al. Ultrathin amorphous cobalt-vanadium hydr (oxy) oxide catalysts for the oxygen evolution reaction. Energy Environ Sci 2018;11:1736–41. https://doi.org/10.1039/C8EE00611C.
[48] Chen H, Ouyang S, Zhao M, Li Y, Jjaam Ye. Synergistic activity of Co and Fe in amorphous Cox-Fe-B catalyst for efficient oxygen evolution reaction. ACS Appl Mater 2017;9:40333–43. https://doi.org/10.1021/acsami.7b13939.
[49] Sivanantham A, Ganesan P, Vinu A, Shanmugam SAC. Surface activation and reconstruction of non-oxide-based catalysts through in situ electrochemical tuning for oxygen evolution reactions in alkaline media. ACS Catal 2019;10:463–93. https://doi.org/10.1021/acscatal.9b04216.
[50] Fang W, Zhu Z, Yu J, Fan W, Hu C, Liu X, et al. First principles study on high-efficient overall water splitting by anchoring cobalt boride with transition metal atoms. Int J Hydrogen Energy 2024;53:1310–22. https://doi.org/10.1016/j.ijhydene.2023.11.347.
[51] Maity T, Roy S. Asymmetric shift of exchange bias loop in Ni-$Ni(OH)_2$ core-shell nanoparticles. J Magn Magn Mater 2018;465:100–5. https://doi.org/10.1016/j.jmmm.2018.05.064.
[52] Lavorato GC, Lima E, Troiani HE, Zysler RD, Winkler EL. Tuning the coercivity and exchange bias by controlling the interface coupling in bimagnetic core/shell nanoparticles. Nanoscale 2017;9:10240–7. https://doi.org/10.1039/C7NR03740F.
[53] Chen RR, Sun Y, Ong SJH, Xi S, Du Y, Liu C, et al. Antiferromagnetic inverse spinel oxide $LiCoVO_4$ with spin-polarized channels for water oxidation. Adv Mater 2020;32:1907976. https://doi.org/10.1002/adma.201907976.
[54] Gracia J. Spin dependent interactions catalyse the oxygen electrochemistry. Phys Chem Chem Phys 2017;19:20451–6. https://doi.org/10.1039/C7CP04289B.
[55] Xue D, Zhao Y, Cao J, Wang Y, Li X, Ma T. Spin engineering of dual-atom site catalysts for efficient electrochemical energy conversion. Adv Mater 2025;37:2504213. https://doi.org/10.1002/adma.202504213.
[56] Vadakkayil A, Clever C, Kunzler KN, Tan S, Bloom BP, Waldeck DH. Chiral electrocatalysts eclipse water splitting metrics through spin control. Nat Commun 2023;14:1067. https://doi.org/10.1038/s41467-023-36703-w.
[57] Liu X, Shi C, Zhang G, Gao R, Pan L, Zhang X, et al. Oxyanions stabilized low-coordinated nickel species for efficient and durable nucleophilic electrooxidation. Nat Commun 2025;16:11224. https://doi.org/10.1038/s41467-025-66298-3.
[58] Li Y, Liu J, Li S, Peng S. Codecoration of phosphate and iron for improving oxygen evolution reaction of layered $Ni(OH)_2$/NiOOH. ACS Catal 2024;14:4807–19. https://doi.org/10.1021/acscatal.4c00229.
[59] Zhang Y, Liang C, Wu J, Liu H, Zhang B, Jiang Z, et al. Recent advances in magnetic field-enhanced electrocatalysis. ACS Appl Energy Mater 2020;3:10303–16. https://doi.org/10.1021/acsaem.0c02104.
[60] Hunt C, Zhang Z, Ocean K, Jansonius RP, Abbas M, Dvorak DJ, et al. Quantification of the effect of an external magnetic field on water oxidation with cobalt oxide anodes. J Am Chem Soc 2022;144:733–9. https://doi.org/10.1021/jacs.1c08759.
[61] Wang J, Sun M, Zhang X, Liu J, He J, Ge W, et al. pH-dependent urea electrooxidation: from mechanism to catalysts and applications. Adv Mater 2026;38:e15043. https://doi.org/10.1002/adma.202515043.
[62] Yang H, Li F, Zhan S, Liu Y, Liu T, Wang L, et al. Metal-hydroxyls mediate intramolecular proton transfer in heterogeneous O-O bond formation. Nat Chem 2026;18:335–44. https://doi.org/10.1038/s41557-025-01993-8.
[63] Xu Y, Mao Z, Zhang J, Ji J, Zou Y, Dong M, et al. Strain-modulated Ru-O covalency in Ru-Sn oxide enabling efficient and stable water oxidation in acidic solution. Angew Chem Int Ed 2024;136:e202316029. https://doi.org/10.1002/anie.202316029.
[64] Zhao H, Zhu L, Yin J, Jin J, Du X, Tan L, et al. Stabilizing lattice oxygen through Mn doping in $NiCo_2O_4$ spinel electrocatalysts for efficient and durable acid oxygen

evolution. Angew Chem Int Ed 2024;63:e202402171. https://doi.org/10.1002/anie.202402171.
[65] Huang Z-F, Song J, Du Y, Xi S, Dou S, Nsanzimana JMV, et al. Chemical and structural origin of lattice oxygen oxidation in Co-Zn oxyhydroxide oxygen evolution electrocatalysts. Nat Energy 2019;4:329–38. https://doi.org/10.1038/s41560-019-0355-9.
[66] Wang X, Xi S, Huang P, Du Y, Zhong H, Wang Q, et al. Pivotal role of reversible NiO_6 geometric conversion in oxygen evolution. Nature 2022;611:702–8. https://doi.org/10.1038/s41586-022-05296-7.